

Robotic volumetric PIV of a full-scale cyclist

Jux, Constantin; Sciacchitano, Andrea; Schneiders, Jan F.G.; Scarano, Fulvio

DOI

[10.1007/s00348-018-2524-1](https://doi.org/10.1007/s00348-018-2524-1)

Publication date

2018

Document Version

Final published version

Published in

Experiments in Fluids: experimental methods and their applications to fluid flow

Citation (APA)

Jux, C., Sciacchitano, A., Schneiders, J. F. G., & Scarano, F. (2018). Robotic volumetric PIV of a full-scale cyclist. *Experiments in Fluids: experimental methods and their applications to fluid flow*, 59(4), Article 74. <https://doi.org/10.1007/s00348-018-2524-1>

Important note

To cite this publication, please use the final published version (if applicable). Please check the document version above.

Copyright

Other than for strictly personal use, it is not permitted to download, forward or distribute the text or part of it, without the consent of the author(s) and/or copyright holder(s), unless the work is under an open content license such as Creative Commons.

Takedown policy

Please contact us and provide details if you believe this document breaches copyrights. We will remove access to the work immediately and investigate your claim.



Robotic volumetric PIV of a full-scale cyclist

Constantin Jux¹ · Andrea Sciacchitano¹ · Jan F. G. Schneiders¹ · Fulvio Scarano¹

Received: 14 September 2017 / Revised: 1 February 2018 / Accepted: 15 March 2018 / Published online: 2 April 2018
© The Author(s) 2018

Abstract

A novel approach to the measurement of large-scale complex aerodynamic flows is presented, based on the combination of coaxial volumetric velocimetry and robotics. Volumetric flow field measurements are obtained to determine the time-averaged properties of the velocity field developing around a three-dimensional full-scale reproduction of a professional cyclist. The working principles of robotic volumetric PIV are discussed on the basis of its main components: helium-filled soap bubbles as tracers; the compact coaxial volumetric velocimeter; a collaborative 6 degrees of freedom robot arm; particle image analysis based on Shake-the-Box algorithm and ensemble statistics to yield data on a Cartesian mesh in the physical domain. The spatial range covered by the robotic velocimeter and its aerodynamic invasiveness are characterised. The system has the potential to perform volumetric measurements in a domain of several cubic metres. The application to the very complex geometry of a full-scale cyclist in time-trial position is performed in a large aerodynamic wind tunnel at a flow speed of 14 m/s. The flow velocity in the near field of the cyclist body is gathered through 450 independent views encompassing a measurement volume of approximately 2 m³. The measurements include hidden regions between the arms and the legs, otherwise very difficult to access by conventional planar or tomographic PIV. The time-averaged velocity field depicts the main flow topology in terms of stagnation points and lines, separation and reattachment lines, trailing vortices and free shear layers. The wall boundary layers developing on the body surface hide below the level resolvable by the present measurements.

1 Introduction

Since its introduction, particle image velocimetry (PIV) has advanced into a versatile technique for aerodynamics research. Although PIV is predominantly used in research laboratories, its application in industrial facilities is broadly documented as indicated in Table 1. Noticeably, all but one of the listed studies (Casper et al. 2016) consider planar two-component or stereoscopic PIV configurations, of which the illumination and imaging systems are mostly mounted on independent traversing systems. Some studies repeat 2D measurements in several planes to gather knowledge across a volumetric domain: Nakagawa et al. (2015) slice the volume downstream of a 28%-scale car model with several horizontal PIV planes. Similarly, Mead et al. (2015) employ

repeated stereoscopic PIV measurements in the validation of noise prediction models, scanning a coaxial jet flow.

Already for stereoscopic PIV configurations the system complexity can be high. The helicopter rotor wake study by Raffel et al. (2004) involves five cameras and three double-pulsed Nd:YAG lasers on a 10-m long and 15-m high traversing system. The measurements of Mead et al. (2015) required a purpose-built gantry to enable the desired multi-plane PIV acquisitions in a coaxial jet flow.

The PIV community feeds the industry demand by supplying tools such as the automatic four-axis traversing system from Intelligent Laser Applications GmbH, enabling fast repositioning of PIV cameras and light sources, complying with the stringent requirements on planar PIV alignments (focussing, Scheimpflug condition, stereoscopic calibration).

The industry preference for multiple planar measurements instead of a full volumetric approach may be twofold; on the one hand, achievable measurement volumes in tomographic PIV (Elsinga et al. 2006) are still fairly limited. The full-scale car study of Wendt and Fülll (2001) shows that even for stereoscopic measurements, multiple FOVs are required to capture the desired domain. One of the largest stereoscopic PIV systems was developed and demonstrated at

Electronic supplementary material The online version of this article (<https://doi.org/10.1007/s00348-018-2524-1>) contains supplementary material, which is available to authorized users.

✉ Andrea Sciacchitano
a.sciacchitano@tudelft.nl

¹ Department of Aerospace Engineering, Delft University of Technology, Delft, The Netherlands

Table 1 Experiments conducted in industrial or large-scale facilities with PIV

| Research group | Measurement configuration | Wind tunnel | Measurement domain size |
|---|--|---|---|
| Pengel et al. (1997), aircraft half-model wake | Planar (two components) | DNW (LLF), Marknesse (NL) | – |
| Coustols et al. (2004), aircraft half-model wake | Ten-camera system with purpose-build support | ONERA (B10), Lille (FR) | 1390×920 mm ² , 1.28 m ² |
| Raffel et al. (2004), rotor trailing vortices | Stereoscopic, four-axis traverse | DNW (LLF), Marknesse (NL) | 460×360 mm ² , 0.17 m ² |
| Jenkins et al. (2009), helicopter rotor wake | Stereoscopic | NASA (14×22), Langley (USA) | 1524×914 mm ² , 1.39 m ² |
| Mead et al. (2015), coaxial jet flow, noise prediction model validation | Stereoscopic, purpose-made gantry traversing system | QinetiQ Ltd noise test facility, Farnborough (GB) | (10×) 350×200 mm ² , (10×) 0.07 m ² |
| Wendt and Fülll (2001), Full-scale Audi A2 car model | Stereoscopic, in-plane traversing | Audi, Ingolstadt (DE) | (3 ×) 540×1600 mm ² , (3×) 0.86 m ² |
| Cardano et al. (2007), full-scale car aerodynamics | Stereoscopic, traversing system | Pininfarina wind tunnel, Turin (IT) | O (1 m ²) |
| Nakagawa et al. (2015), 28% car model | Planar, light source traversed manually (out-of-plane) | Toyota R&D, Aichi (JPN) | (16×) 540×405 mm ² , (16×) 0.22 m ² |
| Casper et al. (2016), full-scale car wake | Tomographic PIV + HFSB, static system | Volkswagen, Wolfsburg (DE) | 2000×1600×200 mm ³ , 0.64 m ³ |
| Toyota Motorsports GmbH, (TMG) (2017), general application in motorsports development | Stereoscopic, traversing system | TMG, Cologne (DE) | 350×350 mm ² , 0.12 m ² |

NASA, where Jenkins et al. (2009) measured a $1.5 \times 0.9 \text{ m}^2$ plane in a rotorcraft wake. Second, the system complexity and data processing burden make the deployment of tomographic PIV at industrial level unlikely in its present form.

The recent introduction of helium-filled soap bubbles (HFSB) for wind tunnel measurements (Scarano et al. 2015) has mitigated the limitations due to the first above point. For instance, Caridi et al. (2015) report a fluid domain of $40 \times 20 \times 20 \text{ cm}^3$ on a tip vortex study of a vertical axis wind turbine. Schanz et al. (2016a) have attained 3D volume measurements of 0.5 m^3 in a confined vessel. Terra et al. (2016) demonstrated wake studies on a cyclist model, capturing a measurement domain of 2 m^2 at 4 m/s free stream velocity.

The complexity of 3D PIV measurements stems from the setup of a multitude of cameras. The calibration of the optical path from the image space to the measurement region in physical space requires a high precision for a successful tomographic reconstruction (Wieneke 2008; Scarano 2013). Combining several configurations or positions is currently unfeasible, given the time and care needed to precisely install the imaging and illumination devices and to re-calibrate them. To date, no work is reported in the literature where tomographic PIV is performed on a multitude of regions for the purpose of covering a complex three-dimensional domain of interest. An additional limitation is identified in the conventional setup of a tomographic PIV system, where the combination of large tomographic aperture angles along with perpendicular volume illumination is

limiting the optical access around complex and especially concave objects. Finally, not least, repeated experiments with tomographic PIV are hampered by the computational burden associated with the tomographic reconstruction and volume interrogation based on spatial cross-correlation. The recent introduction of particle-based reconstruction techniques (IPR, Wieneke 2012 among others) combined with an efficient tracking algorithm (Shake-the-Box, Schanz et al. 2016b) has reduced the computational burden by orders of magnitude.

The coaxial volumetric velocimeter (CVV), recently introduced by Schneiders et al. (2018), is a compact measurement device that has the potential to exploit the full advantage of robotic manipulation. Large-scale PIV measurements around complex objects require the superposition of a multitude (often hundreds) of observation domains along different directions. The latter can only be approached by the operation of a three-dimensional measurement system that does not require calibration after repositioning of the measurement probe.

Based on the above premises, a robotic approach is presently investigated, whereby a mechanical arm simultaneously controls the probe position and orientation, while delivering the position data to allow spatial recombination of the measured regions. With this technique, the CVV probe is immersed in the flow and its disturbing effect needs to be carefully scrutinized. The data processing cannot follow the typical chain of tomographic PIV, due to the large computational cost. Instead, the more efficient Lagrangian particle

tracking technique (Shake-the-Box, Schanz et al. 2016b) is adopted.

The present work illustrates the potential of the sought measurement approach with an experiment, where the time-averaged near flow field around a full-scale cyclist (3D replica of Olympic silver medallist Tom Dumoulin, as used by Terra et al. 2016) is obtained. The measurements entail 450 measurement regions combined within a flow domain of more than 2 m^3 . The investigation features the measurements within intricate three-dimensional regions of difficult optical access (chest–arms cavity, intra-leg region, ankle–feet, among others) requiring several observation directions, which could hardly be accessed by planar or conventional tomographic PIV.

The experimental apparatus and the integration of the robotic system within the open jet facility at TU Delft are described. Details of the measurement procedure are discussed with attention to the main properties of the data delivered within the experiments, such as spatial resolution, measurement uncertainty, duration of wind tunnel tests and of data processing. The work concludes describing the main physical properties of the flow developing around the cyclist, in terms of velocity field topology (stagnation, separation and reattachment lines) and shear and vorticity dynamics (shear layers, trailing vortices and their interactions).

2 Working principles

The robotic PIV approach realizes multiple 3D velocity measurements with coaxial volumetric velocimetry (CVV, Schneiders et al. 2018) and combines them into a single domain discretized by cubic cells. A specific advantage of coaxial velocimetry is its superior optical access to complex geometries such as concave or enclosed regions (Sect. 2.1). The principles of CVV are summarized here for completeness. A specific discussion of the aerodynamic impact of the probe when inserted in the flow is given (Sect. 2.2). The position and orientation of the CVV probe is controlled by means of a robotic arm. Details on the robot hardware and the required data mapping between individual frames of reference are discussed (Sect. 2.3). The combination of the novel CVV probe and the robotic arm requires dedicated measurement and data processing procedures (Sect. 2.4), such as the rotation and merging of datasets, specific averaging techniques and the determination of achievable spatial resolution.

2.1 Optical access in PIV

A brief discussion on optical access is given here. The topic of optical access is barely discussed in the literature, as each experiment poses its specific challenges. A general

observation is that the access by PIV to a fluid domain close to and all around complex, non-transparent geometries requires multiple illumination and imaging directions. This is often achieved partitioning the fluid domain, for instance scanning the measurement plane along the direction perpendicular to it. A limiting factor in such cases is the relative angle spanned between the imaging and the illumination system, hereafter referred to as α . This can be illustrated in a simple example, assuming the flow around a cylinder.

In the planar PIV configuration with the light sheet normal to the imaging direction, the object obstructs the imager's field of view, while also shadowing the light sheet (Fig. 1a). Thus, a single viewing and illumination direction does not suffice for the purpose of measuring the flow in the shadowed regions. If volumetric data are desired, the volume is further to be sliced with multiple planar measurements.

Using tomographic PIV eliminates the need to scan the position of the measurement plane. However, the angle α spanned by the imaging and illumination system in Fig. 1b is even larger and consequently, the shadowed area erodes more significantly the measurement domain. Thus, also tomographic PIV requires multiple imaging and illumination directions to gather a 360° view of the cylinder flow. Given the higher complexity in setting up the tomographic imaging systems and the associated calibration procedure (volume self-calibration, Wieneke 2008), performing tomographic PIV measurements along different views is rarely pursued in view of time and complexity of the measurements.

The CVV approach is characterised by collinear illumination and imaging (Fig. 1c). The shadowed region is approximately prismatic or cylindrical and two views rotated by a large angle will suffice to capture the full volume. The compact arrangement of the PIV hardware in this configuration simplifies its movement as a whole and enables its position control with a robotic arm. Compared to single-point measurements based on multi-hole pressure probes and hot-wire anemometry, the CVV approach offers the advantage that measurements of the full velocity vector can be obtained even in the presence of reverse flow and in proximity of solid surfaces. Moreover, it should be noted that measurements based on probes are intrusive in that the probe interacts with the flow at the point of measurement. The coaxial velocimeter instead measures the flow velocity starting from a distance of approximately 20 cm. The aerodynamic effect of the velocimeter on the flow is discussed in Sect. 2.2.2.

2.2 Coaxial volumetric velocimetry

The working principle of CVV (Schneiders et al. 2018) is akin to tomographic PIV (Elsinga et al. 2006). Alignment of the imaging and illumination axes with four cameras at considerably lower tomographic aperture (Fig. 2) as compared

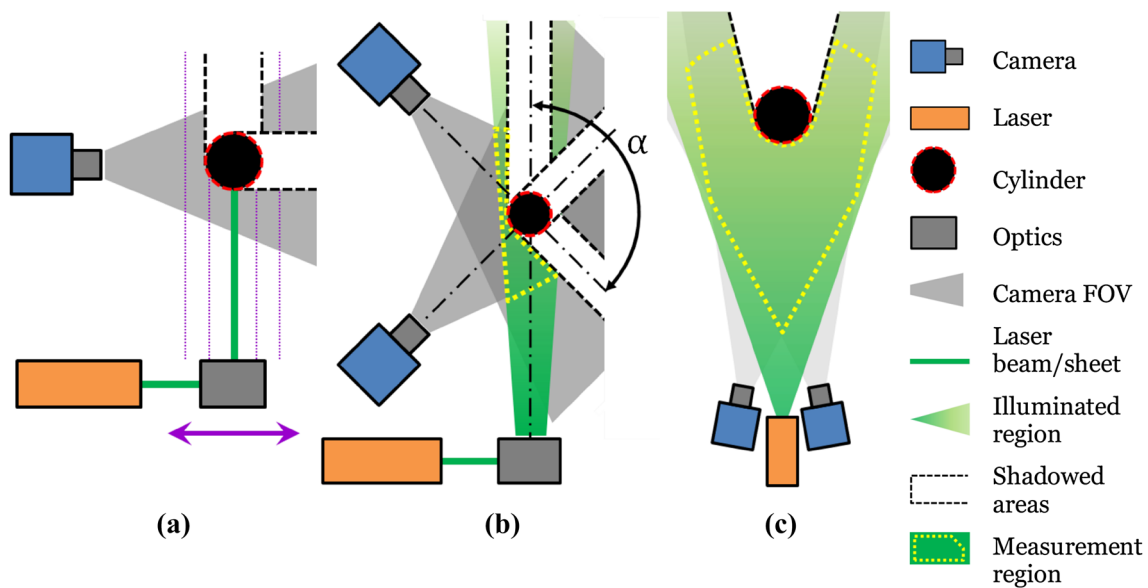


Fig. 1 Optical access for different PIV configurations in case of cylinder flow. Illuminated regions are indicated in green, camera field of view shaded in grey. White regions with black dashed contours mark the shadowed domains. **a** Planar PIV. Purple arrow and dotted lines

indicate volume scanning approach. **b** Tomographic PIV. Dashed yellow lines indicate actual measurement domain. **c** Coaxial volumetric velocimetry

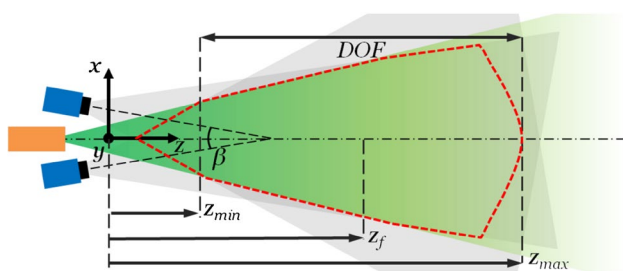


Fig. 2 2D illustration of coaxial volumetric velocimetry including reference frame definition, reproduced from Schneiders et al. (2018). Cameras (blue) at tomographic aperture angle β in a coaxial arrangement with the laser light source (orange). Illumination volume indicated in green, whereas field of view is grey. The overlap of the latter defines the measurement region outlined in dashed red

to the setup used in tomographic PIV experiments yields unique imaging characteristics as discussed hereafter.

2.2.1 Coaxial imaging

The measurement volume depth resulting from the CVV arrangement typically exceeds the volume width and height, as opposed to the situation encountered with thin or thick sheet measurements in tomographic PIV. The depth of field (DOF) may reach well up to 1 m and implies considerable variations of the particle imaging properties along the depth direction (z).

Particle detection and tracking probability is maximized when particle images are formed in focus. This condition requires a depth of field encompassing the full depth of the measurement domain. It follows that for a large depth of field, a high $f_{\#}$ (low numerical aperture) is necessary,

$$DOF \propto f_{\#}^2 \tag{1}$$

which limits the amount of light received by the camera.

The particle image displacement of the tracer at velocity u is inversely proportional to the distance z . The variation is due to the optical magnification M being inversely proportional to the object distance z ($M \times z = \text{const}$). It is noted that in the nominal working range, particle images recorded in the CVV configuration are diffraction limited.

In the above conditions, the particle image intensity of the coaxial imaging and illumination arrangement obeys an inverse fourth-order relation with object distance (Schneiders et al. 2018), that is,

$$I_p \propto z^{-4} \tag{2}$$

It follows that the maximum measurement distance z_{max} is limited by the relative particle image intensity with respect to the detector noise level. Conversely, the closest distance where measurements are still valid, z_{min} , is limited by the aerodynamic interference between the coaxial velocimeter head and the flow.

2.2.2 Aerodynamic interference

Modelling the velocimeter as a sphere and seeking the 3D potential flow solution as a first approximation of aerodynamic interference provides justification for a minimum distance z_{\min} . Considering a freestream V_∞ in spherical coordinates

$$V_{r_0} = V_\infty \cos \theta \quad V_{\theta_0} = -V_\infty \sin \theta \quad V_{\phi_0} = 0 \quad (3)$$

and adding a doublet to model the flow around a sphere of radius R , the potential velocity field around the sphere is described by,

$$V_r = V_\infty \left(1 - \frac{R^3}{r^3} \right) \cos \theta \quad (4)$$

$$V_\theta = -V_\infty \left(1 + \frac{R^3}{2r^3} \right) \sin \theta \quad (5)$$

$$V_\phi = 0 \quad (6)$$

where r is the radial distance to the sphere centre. Comparing Eqs. 4 and 5, it is observed that the disturbance of both radial and tangential velocity component decays with r^{-3} . Quantifying the induced velocity deviation induced by the sphere as

$$\epsilon_V = \frac{\sqrt{(V_r - V_{r_0})^2 + (V_\theta - V_{\theta_0})^2}}{V_\infty} \quad (7)$$

results in elliptical iso-lines of induced velocity error ϵ_V with the major axis aligned with the freestream, as shown in Fig. 3. In the assumption that the probe is not directly upstream of the region of interest ($\theta > \pi/2$), the velocity perturbation is least significant along the y-axis ($\theta = \pi/2$). For a given radial distance r , the error ϵ_V increases with increasing θ beyond $\theta = \pi/2$.

Considering a nominal working range of $\pi/2 < \theta < 5\pi/6$, in the best case scenario ($\theta = \pi/2$) the error ϵ_V stays below 1% for $r > 3.7R$. In the worst case ($\theta = 5\pi/6$), it can be shown that for a given r , the relative error ϵ_V is 1.8 times higher. Along this viewing direction the 1% mark is reached at $r = 4.5R$.

The coaxial velocimeter used in the present work is modelled with a sphere of 10 cm diameter ($R = 5$ cm) based on cross-sectional equivalence. Allowing for a maximum velocity disturbance of 1%, a minimum measurement distance of $z_{\min} = 17.5$ cm must be respected.

The prediction of flow disturbance based on potential flow theory is compared with the freestream measurements conducted in side-viewing condition ($\theta = \pi/2$, Fig. 3). The results show an acceptable agreement in terms of flow deflection and acceleration caused by the measurement probe.

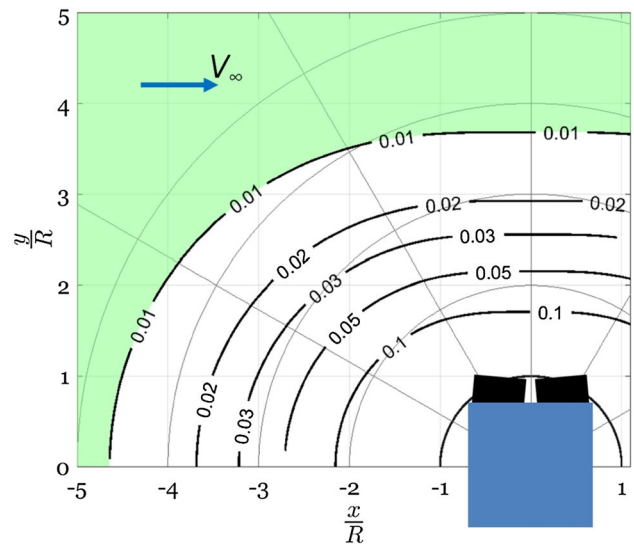


Fig. 3 Contours of ϵ_V induced by the presence of a sphere with radius R , assuming a potential flow solution. Freestream V_∞ as defined in Eq. 3 with $x = r \cos \theta$ and $y = r \sin \theta$. Green area indicates valid measurement region for $\epsilon_V < 1\%$

2.3 Collaborative robotic arm

Collaborative robots are robotic devices that manipulate objects in collaboration with a human operator (Colgate et al. 1996). Robotic handling is suited for controlled and rapid coverage of the complete measurement domain by partitioning it into a number of local 3D measurements. The robot tool end, herein referred to as the robot hand, holds the CVV probe and controls its position and orientation. At each position, the 3D PIV measurement obtained by the CVV probe yields the time-averaged velocity field in the ‘robot hand reference frame’ ($x_{\text{rh}}, y_{\text{rh}}, z_{\text{rh}}$). Note that the latter corresponds to the reference frame of the velocimeter (‘c’) indicated in Fig. 2, offset by a known distance \vec{x}_{cor} ($\vec{x}_{\text{rh}} = \vec{x}_c - \vec{x}_{\text{cor}}$). Translating (\vec{x}_i) and rotating the robot hand along roll, pitch and yaw (α, β, γ) allows selecting different regions of the flow to be inspected, or to observe the same region from a different viewing direction in case of obstructed view or unwanted reflections. The probe position is controlled with respect to its base position, indicated by the point P_b in Fig. 4. This provides the necessary information to map the measurement data onto a global (‘g’) frame of reference related to the object or the wind tunnel. Then,

$$M_x = \begin{bmatrix} 1 & 0 & 0 \\ 0 & \cos \beta & \sin \beta \\ 0 & -\sin \beta & \cos \beta \end{bmatrix} \quad M_y = \begin{bmatrix} \cos \gamma & 0 & -\sin \gamma \\ 0 & 1 & 0 \\ \sin \gamma & 0 & \cos \gamma \end{bmatrix} \quad (8)$$

$$M_z = \begin{bmatrix} \cos \alpha & \sin \alpha & 0 \\ -\sin \alpha & \cos \alpha & 0 \\ 0 & 0 & 1 \end{bmatrix}$$

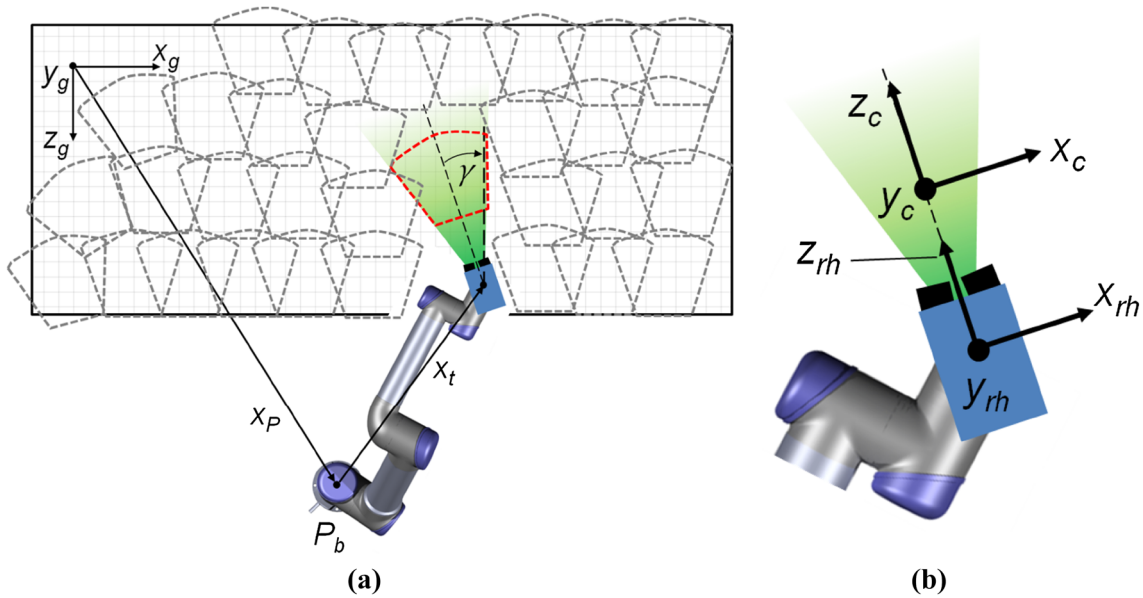


Fig. 4 Illustration of reference frames and concept of domain partitioning. Specifics on actual robot arm detailed in Sect. 3.3. **a** Global reference frame with arbitrary region of interest. Potential measurement volumes outlined to illustrate concept of domain partitioning

(animated view of measurement domain formation is available in video 1). **b** Robot hand holding the CVV with indication of reference frames

$$\vec{x}_g = (\vec{x}_{rh})(M_x M_z M_y) + \vec{x}_P + \vec{x}_t \tag{9}$$

$$\vec{u}_g = (M_y M_z M_x) \vec{u}_{rh} \tag{10}$$

where M_i represents the rotation matrices around the i -axes and \vec{x}_g, \vec{u}_g are the position and velocity in the global reference frame. A simplified view of the layout is shown in Fig. 4.

2.4 Data acquisition and processing

The motion of the particle tracers is evaluated using the Shake the Box (STB) algorithm (Schanz et al. 2016b) implemented in the LaVision DAVIS 8 software. The Lagrangian particle tracking procedure is computationally efficient, while allowing for reliable particle tracking in densely seeded flows, yielding advantages in computational time and velocity dynamic range, when compared to tomographic PIV. For each HFSB tracer particle, the position \vec{x}_{rh} along a trajectory is sampled several times, yielding its velocity vector \vec{u}_{rh} at a given time step t_i .

For the robotic CVV system used in the present experiment, the particle tracks are first reconstructed within the reference system of the local measurement (x_{rh}, y_{rh}, z_{rh}) . The spatially randomly distributed particle data are expressed through coordinates transformation in the global system of reference, where the ensemble statistics for each cell are evaluated.

Data within a finite time interval and spatial range are included in each cell, where the results are then temporally and spatially averaged. Although several spatial averaging approaches have been proposed for particle-based techniques (e.g. Agüera et al. 2016), ensemble averaging is applied here in both space and time over cubic regions of space (cells), which is a simple and computationally efficient option for the large data set. The time-averaged velocity estimator reads as

$$\bar{u}_a = \frac{1}{N} \sum_{i=1}^N \vec{u}_i \quad \text{with } x, y, z \in \text{cell } a \tag{10}$$

where N is the number of instantaneous samples u_i captured inside the cell a . The spatial variations of velocity within the cell are neglected within this approach, assuming that the cell size is chosen small enough to prevent spatial modulation of the velocity distribution. Yet, the measurement cell must include a sufficiently large number of samples to return a representative average value, given that the uncertainty $\epsilon_{\bar{u}}$ reduces with $N^{-0.5}$. In the generic hypothesis of unsteady/turbulent flows, the measurement uncertainty $\epsilon_{\bar{u}}$ of the mean velocity estimation \bar{u} is

$$\epsilon_{\bar{u}} = \frac{k\sigma_{\bar{u}}}{\sqrt{N}} \tag{12}$$

where N indicates the number of measurement samples included in the cell assuming they are uncorrelated and follow a Gaussian distribution. The confidence interval is accounted by the coverage factor k . For a desired uncertainty level $\varepsilon_{\bar{u}}$, a known velocity standard deviation $\sigma_{\bar{u}}$ and coverage k , the minimum sample size N_{\min} can be selected.

In the present work a minimum volume for the linear size of the measurement cell is derived from the selection of N_{\min} and the seeding concentration C .

$$l_V = \sqrt[3]{\frac{N_{\min}}{n \cdot C}} \tag{13}$$

For a cubic cell of length l_V and n uncorrelated velocity samples the dynamic spatial range of the time-averaged velocity is estimated by,

$$DSR = \frac{L}{l_V} = L \left(\frac{n \cdot C}{N_{\min}} \right)^{\frac{1}{3}} \tag{14}$$

where L is the length of the overall measurement domain.

3 Experimental apparatus and procedures

Wind tunnel measurements are conducted at the open jet facility of TU Delft, where the flow behaviour around the full-scale replica of the professional cyclist Tom Dumoulin (Terra et al. 2016) is studied by means of robotic PIV. Experiments are carried out at a Reynolds number of 5.5×10^5 , based on the cyclist’s torso length (600 mm). The facility and the cyclist model are introduced in Sects. 3.1 and 3.2, respectively. The specific hardware and its performance are discussed in the following section, including the HFSB seeding system (Sect. 3.3.1), the coaxial volumetric velocimetry probe (Sect. 3.3.2) and the robotic arm (Sect. 3.3.3). Specific acquisition procedures are outlined in Sect. 3.4.

3.1 Open jet facility (OJF)

The open jet facility at the Wind Tunnel Laboratories of TU Delft features an atmospheric closed-loop, open jet wind tunnel with a contraction ratio of 3:1 and an octagonal exit section of $2.85 \times 2.85 \text{ m}^2$. The fan controlling the flow speed is driven by a 500 kW electrical motor. The wind speed ranges from 4 to 35 m/s. The jet stream is bounded by shear layers spreading with a semi-angle of 4.7° (Lignarolo et al. 2014). During the measurements, the wind speed is held constant at 14 m/s. A heat exchanger downstream of the test section maintains a constant air temperature independent of the flow speed. The turbulence intensity of the free stream is reported to be 0.5% (Lignarolo et al. 2014). The latter does not include the aerodynamic effects of the seeding generator

upstream of the cyclist, which raises the turbulence intensity. Some discussion is given in Sect. 3.3.1.

3.2 Cyclist model

The need to achieve test repeatability and to cope with potential risks of laser illumination motivates wind tunnel testing with replica models rather than the human athletes. To maintain a steady position of the athlete for the complete measurement duration, an additively manufactured full-scale replica of the time trialling top athlete Tom Dumoulin (Terra et al. 2016) is installed in the test section (Fig. 5). The static mannequin obeys a fixed crank angle of 75° as detailed in Table 2 which summarizes the characteristic model dimensions. As discussed in Crouch et al. (2016), the use of a static model yields a wake flow that is highly representative of the phase-averaged flow field of a pedalling athlete, while greatly simplifying the experimental setup.

The cyclist wears a long-sleeve Etxeondo time trial suit along with a Giant time trial helmet, as used by Team Giant Alpecin during the 2016 season. The rider is placed on a Giant Trinity Advanced Pro frame equipped with a Shimano

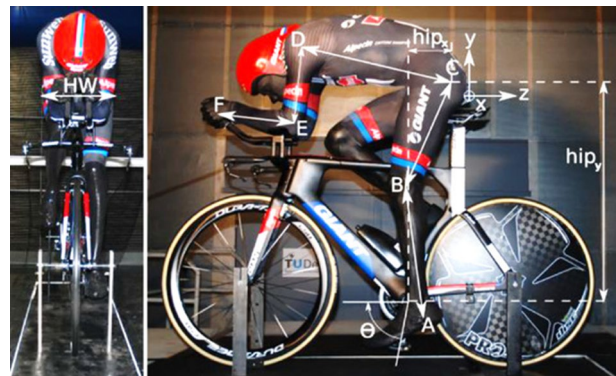


Fig. 5 Cyclist mannequin in front (left) and side view (right) with indication of characteristic dimensions

Table 2 Characteristic mannequin dimensions

| Crank angle | θ | 75° (mm) |
|-------------------|----------|-----------------|
| Hip width | HW | 365 |
| Shoulder width | SW | 380 |
| Hip location, x | hip_x | 180 |
| Hip location, y | hip_y | 850 |
| Shank length | A–B | 475 |
| Thigh length | B–C | 460 |
| Torso length | C–D | 600 |
| Upper arm length | D–E | 326 |
| Forearm length | E–F | 290 |

DuraAce C75 front and a Pro Textreme disc rear wheel, both fitted with 25 mm tubular tires. Rigid supports at front and rear axle connect the bike to a 4.9 m-long and 3.0 m-wide wooden table, placed 0.2 m above the lowest point of the wind tunnel contraction exit. The front wheel centre line is located 2.1 m downstream of the contraction exit.

3.3 Robotic PIV system

The robotic PIV system comprises three major components: the HFSB seeding generator, the coaxial volumetric velocimeter including the illumination unit, and further the robotic arm.

3.3.1 HFSB seeding

Neutrally buoyant HFSB with 400 μm mean diameter are employed as flow tracers. An in-house developed four-wing seeding rake comprising 80 HFSB generators is installed on a two-axis traversing system at the exit of the wind tunnel contraction. The pitch between generators is 5 and 2.5 cm across and along the wings respectively. The system delivers approximately 2×10^6 tracers per second, distributed over a cross section of $15 \times 48 \text{ cm}^2$. The seeding generator shown in Fig. 6 is controlled through a LaVision fluid supply unit.

In the assumption of straight flow through the seeding generator, each nozzle seeds a cross section of 12.5 cm^2 based on the nozzle pitch. At a freestream velocity of 14.0 m/s the seeding concentration of the undisturbed flow C_{HFSB} can be estimated as (Caridi et al. 2016):

$$C_{\text{HFSB}} = \frac{\dot{N}}{\dot{V}} = \frac{25,000 \frac{\text{tracers}}{\text{s}}}{17,500 \frac{\text{cm}^3}{\text{s}}} = 1.43 \frac{\text{tracers}}{\text{cm}^3} \quad (15)$$

where \dot{N} is the production rate of an individual generator and \dot{V} is the volume flow rate across the area delimited by

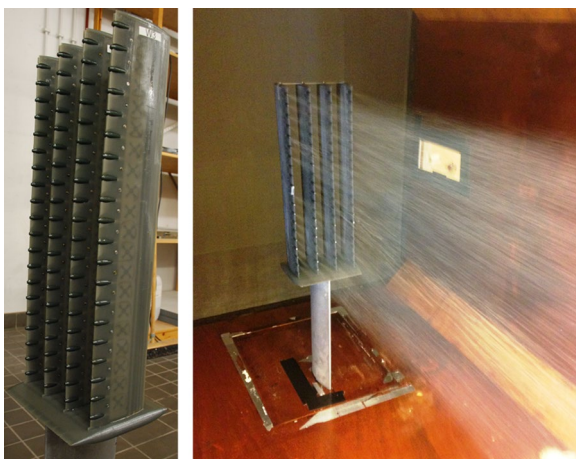


Fig. 6 HFSB seeding system (left) and the seeded stream-tube (right)

neighbouring generators. The aerodynamic invasiveness of the seeding generator is studied by means of a freestream measurement 2 m downstream of the contraction exit using the robotic PIV system. A turbulence intensity of 1.9% is measured in the wake of the region downstream of the rake of wings hosting the generators; conversely, it has been observed that the seeding rake does not affect the mean velocity to a measurable extent. It is noted that the freestream turbulence can be reduced below 1% by placing the seeding rake more upstream inside the wind tunnels settling chamber. The effect of the supporting strut is neglected, given that its wake region is not included in the PIV measurements.

3.3.2 Coaxial volumetric velocimetry probe

Technical specifications of the LaVision CVV probe comprising four CMOS cameras are tabulated in Table 3, together with an illustration of the device in Fig. 7.

Table 3 Technical specifications of coaxial volumetric velocimetry probe

| Housing | Size | $w \times h \times d$ | 131 × 90 × 83 mm |
|--------------|-----------------------|-----------------------|------------------------------------|
| Optics | Focal length | f_i | 4 mm |
| | Numerical aperture | $f_\#$ | 8 |
| Imaging | Tomographic aperture | β | 4° at $z_0 = 40 \text{ cm}$ |
| | Active sensor | $S_x \times S_y$ | $640 \times 475 \text{ px}$ |
| | Pixel pitch | Δ_{px} | 4.8 μm |
| | Bit depth | b | 10 bits |
| Illumination | Acquisition frequency | f | 758 Hz |
| | Pulse energy | E_p | 21 mJ |
| | Wavelength | λ | 527 nm |

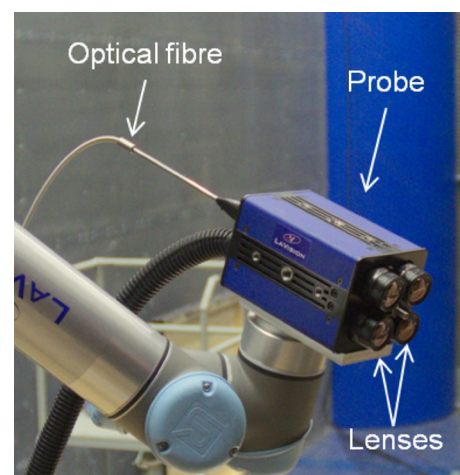


Fig. 7 The coaxial volumetric velocimetry probe comprising four cameras and an optical fibre. The device is held by a robotic arm

Illumination is provided by a Quantronix Darwin Duo Nd:YLF laser, coupled with a spherical, converging 20 mm lens to direct the light beam into a 4 m long optical fibre. Another 4 mm spherical, diverging lens is attached at the fibre end to obtain the desired light spreading angle.

The measurable volume, assuming the absence of objects and sufficient seeding, is bound within the region where the camera views overlap in lateral and vertical direction, whereas the maximum depth is constrained by the relative particle light intensity with respect to the image noise level. At a measurement distance of $z = 20$ cm, the FOV attains 8×13 cm² which extends to 25×40 cm² at $z = 60$ cm. In a separate experiment, the maximum measurement depth is recorded at $z_{\max} = 75$ cm. Figure 8 shows particle tracks recorded in the sample measurement.

3.3.3 Robotic arm

The velocimeter’s position and orientation is controlled by a Universal Robots-UR5 robotic arm. The latter provides motion with six degrees of freedom, similar to the movement range of a human arm, see Fig. 9. The robot base features a single degree of freedom joint, which connects to the so-called shoulder joint, providing the second degree of freedom. The third joint connects the two robot arms in analogy to an elbow. Three more rotation axes at the end of the second arm mimic the articulation of a wrist. The latter connects to the support flange, herein referred to as the robot hand, which holds the CVV probe. The maximum reach of the UR5 stretches 85 cm in radius around its base.

The position and direction of the CVV probe is set by moving the collaborative robot manually aiming at a target point specified on a digital display. The position repeatability is reported as ± 0.1 mm from the manufacturer (Universal Robots 2014).

The robot is installed in two symmetric base positions, each at a height of 65 cm, 90 cm lateral distance to the wheel line and 30 cm downstream of the front wheel centre line.

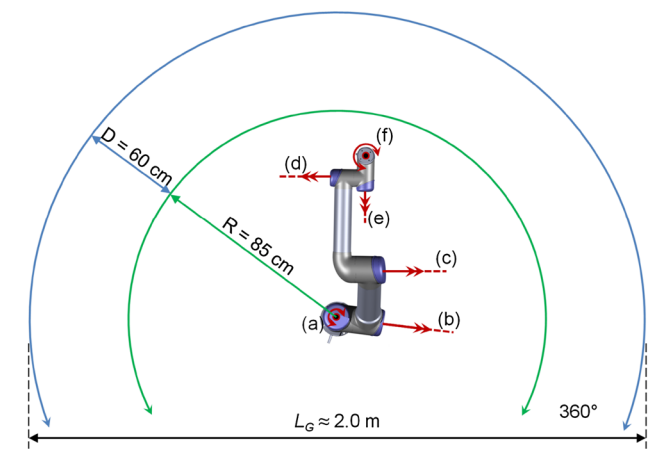
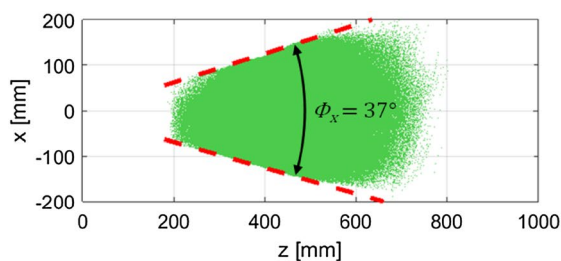


Fig. 9 Robot arm and its active range R . Robot joints labelled as: **a** base, **b** shoulder, **c** elbow and **d–f** wrist. Degrees of freedom indicated in red. The CVV measurement range adds the depth D to the robot range. Drawing not to scale

The overall experimental arrangement is illustrated in Fig. 10. A dynamical illustration of the robot in operation is provided in video 2.

3.4 System calibration and data acquisition procedures

The intrinsic calibration of the CVV follows the same procedure as that for tomographic PIV, consisting of a geometric calibration (Soloff et al. 1997) followed by a volume self-calibration (Wieneke 2008), with the additional requirement that the optical response function is experimentally determined (OTF calibration, Schanz et al. 2012). The latter is necessary to employ the Shake-the-Box algorithm for tracers motion analysis (Schanz et al. 2016b). Once performed, the calibration pertains to the CVV system and does not need to be repeated (universal calibration). Furthermore, transforming the velocity measurements from the individual volumetric domains towards the global coordinate system requires the coefficients appearing in Eqs. 8–10 to be determined.

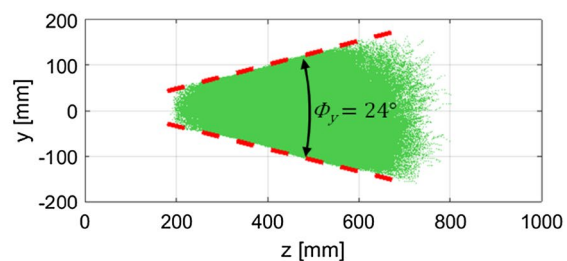
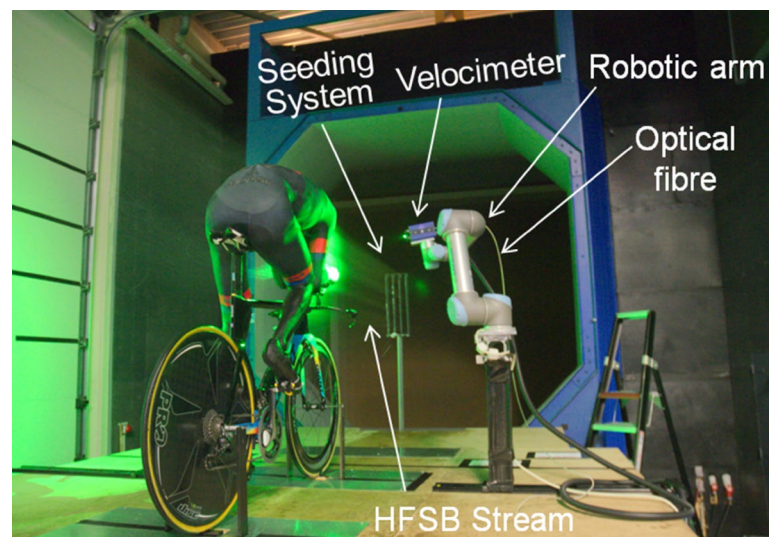


Fig. 8 Particle tracks recorded in 5000 time frames with the CVV probe specified in Table 3

Fig. 10 Experimental setup in OJF, with cyclist, seeding generator, and CVV operated from the robot hand. (further details are illustrated in video 2)



A calibration procedure determines the relative distance between the robot hand and the origin of the measurement domain. Such calibration is performed imaging and reconstructing known targets from different views. Lastly, the position of the robot hand in the global coordinate system is evaluated by imaging a marker in the origin of the latter coordinate system.

For particle image recording the probe is placed in a chosen position. In the present study, measurements are gathered from a total of 450 different positions of the CVV probe. At each position, 5000 images are recorded at a rate of 758 Hz. The system is operated in manual mode by a single-user, where each measurement region requires approximately 2 min. A limiting factor is the user interaction time needed to verify the good positioning of the individual probe. Additional factors affecting the measurement time

are the start-up period of the seeding generator and the data storage time.

The raw particle image recordings are pre-processed with a temporal high-pass filter (Sciacchitano and Scarano 2014), which eliminates most background illumination (see Fig. 11). The pre-processed images are analysed with the Shake-the-Box algorithm (Schanz et al. 2016b), yielding particle tracks with instantaneous velocity vectors at the scattered particle locations.

A total of approximately 10,000 particles is captured in each recording, corresponding to a tracers concentration of ~ 1 particle/cm³ and a particle image density of 0.01 particles per pixel. The actual concentration of tracers can vary in the measurement domain and it is typically below the nominal value established in Eq. 15. About one-tenth of the detected particles are tracked continuously along at least

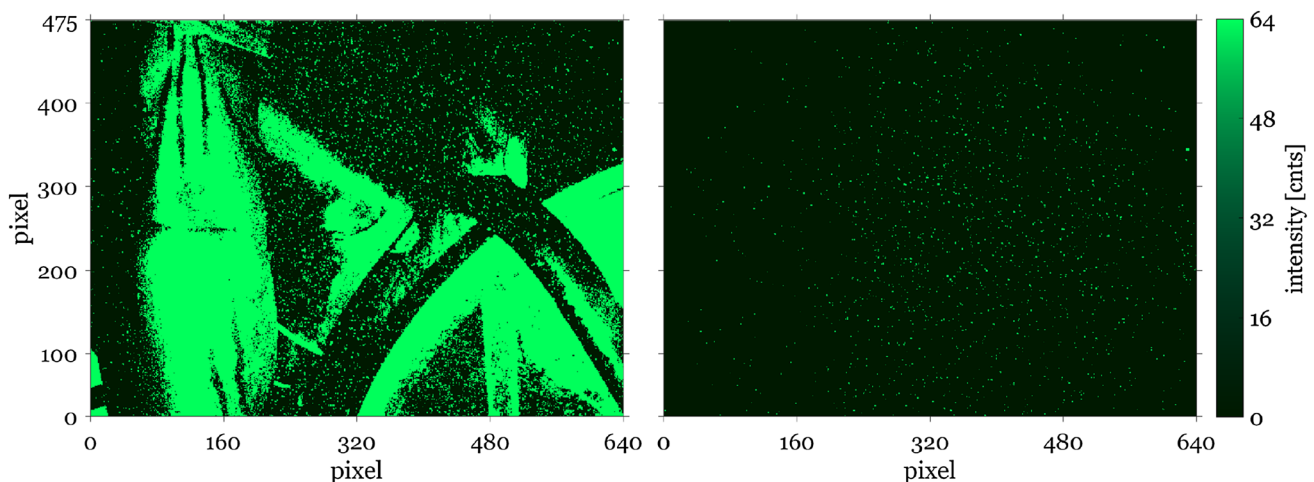


Fig. 11 Illustration of a recording with the CVV system. Left: instantaneous raw image. Right: image after pre-processing with a high-pass Butterworth filter

four recordings, yielding around 1000 particle tracks in each recording. The low tracking rate is ascribed in this case with the large distance travelled by the particles between subsequent recordings. In the free stream, a particle moves approximately 20 mm between two frames. At an object distance of $z=40$ cm, this corresponds to approximately 40 pixels displacement. Particle tracks are typically obtained with 11 samples of the tracer position along its trajectory.

The scattered velocity data obtained at each measurement position are visualized by particle trajectories sampled over a discrete set of time instants (tracks). For the sake of example, Fig. 12 visualizes the cloud of measured data in a region where the optical access is constrained by the mannequin geometry (region between the riders face and his arms). The position of the CVV can be inferred from the pyramidal shape of the measured region.

The overall experiment is composed of 450 likewise measurements where the CVV is pointed around the cyclist mannequin to map the entire flow field in its vicinity. The total number of particle tracking velocity measurements is approximately 1.3×10^9 , which is then statistically evaluated to return the time-averaged velocity vector field. The scattered velocity data are mapped onto the global reference frame. The velocity of tracers falling within each cubic cell (of length $l_V=20$ mm) belongs to the ensemble yielding the time-averaged velocity for the given cell.

The measurements spanning a domain of $2000 \times 1600 \times 700$ mm³ are distributed on a Cartesian grid, where the velocity is described by $400 \times 320 \times 140$ points (cells average is evaluated with 75% overlap) and 5 mm vector spacing. The grid cell size is determined with the criterion that at least ten valid data should be in the ensemble ($N_{\min}=10$). The minimum cell size is limited by the lower seeding concentration in the separated flow behind

the bluff regions of the athlete. Overall, each bin contains on the order of 100 particles on average. For the given settings, a measurement spatial dynamic range $DSR=100$ is attained as the ratio between domain size $L_G=2000$ mm and cell size $l_V=20$ mm.

For the velocity dynamic range (DVR) a value of 100 is estimated, based on the average number of particles per bin and assuming turbulent fluctuations of 10% amplitude relative to the free stream velocity.

The data in the overlapping region of adjacent volumes are used to quantify the measurement uncertainty. The discrepancies on the mean velocity are of the order of 2% for the x - and y -velocity components and 4% for the z -velocity component.

4 Results and discussion

4.1 Global features of velocity distribution

The time-averaged velocity field of the flow around the cyclist is illustrated in Fig. 13 and visualized in more views in the supplemental material (video 3). The velocity contours in the median xy -plane reveal the velocity pattern at the largest scale. The first stagnation region is at the rider's helmet. The flow accelerates along the upper curved back, reaching a maximum at approximately half the torso length. Further downstream, the flow decelerates due to the adverse pressure gradient. The unstable boundary layer undergoes separation at the lower back. The separated region has a relatively small extent and is terminated by a saddle point where streamlines converge right below the bicycle saddle. A secondary stagnation at the front of the rider is identified in the hand region, which has a relatively close position optimized for time-trial. After stagnating, the flow accelerates around the arms and

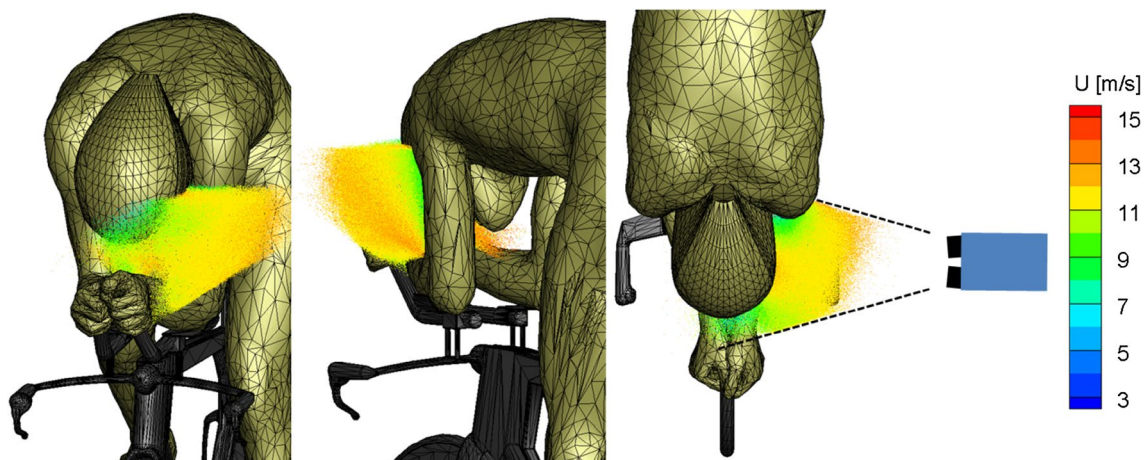
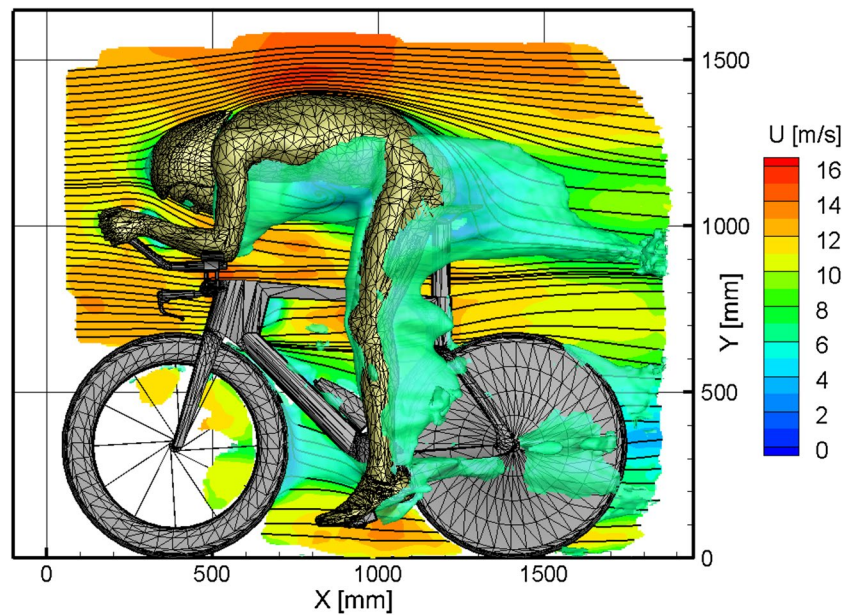


Fig. 12 Scattered particle data colour-coded by streamwise velocity component. The ensemble is obtained from 1000 recordings taken from a single position of the robot hand (right figure)

Fig. 13 Time-averaged velocity field at $u_\infty = 14$ m/s ($Re = 5.5 \times 10^5$) visualized by a contour plane of streamwise velocity u in the centre plane ($z = 0$ mm) including surface streamlines, together with an iso-surface of $u = 7$ m/s



in the structure between the steering and the upper edge of the fork. The analysis of velocity contours and streamlines does not allow the evaluation of the features far from the median plane and of the three-dimensional structures. For this, purpose the 3D iso-surface of streamwise velocity $u = 7$ m/s ($0.5 u_\infty$) is meant to identify the regions where the momentum deficit is most pronounced. The caveat is that flow deceleration around forward stagnation is not considered as it is not relevant to the process of pressure losses by flow separation. Regions where forward stagnation is observed are the front side of the helmet, the upper arms, the entire upper (extended) leg and part of the lower legs.

The two most extended regions exhibiting velocity deficit are a large part of the decelerated flow comprised between the chest, the elbows and the pelvis and the separated flow at the lower back of the cyclist.

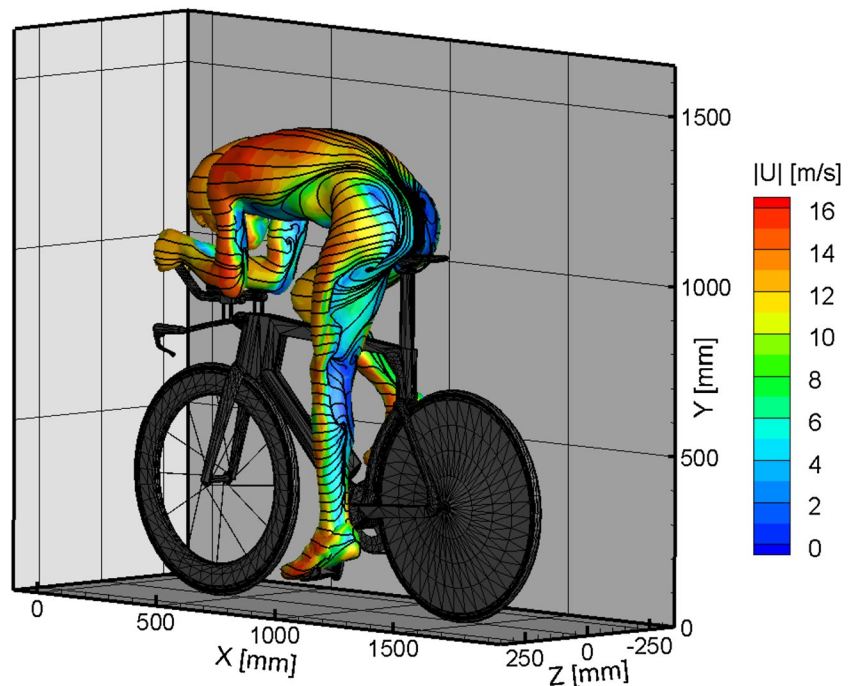
The flow decelerating around pelvis develops sidewise enveloping the hip of the stretched leg. The wake from the leg connects in a three-dimensional topology to the separated region at the rider's low back. The wake region of the latter contracts slightly approaching the knee and becomes again more pronounced in the calf region and past the foot. Finally, some more pronounced region of velocity deficit with streamwise elongation is observed at the heel of foot signalling the presence of streamwise vortices. The visible deceleration closer to the back wheel may be partly accentuated by the presence of the necessary structure to support the model in the wind tunnel. The (non rotating) wheels exhibit a similar wake. The front wheel has its wake centred at the most downstream point, whereas the back wheel has its wake in a slightly upper position.

4.2 Near-surface flow topology

The availability of velocity data around and in the vicinity of the cyclist body surface is used to estimate the topology of skin friction lines. The latter are notably of difficult detection with PIV over curved surfaces due to the challenge of following the surface contour in 3D with the illumination. An excellent example is given in the work of Depardon et al. (2005), where planar PIV measurements 0.5 mm close to the wall have been used to estimate the detailed topology of skin friction lines around a cubic obstacle mounted on a flat plate. The same technique could not be used in this case, due to the complex 3D geometry under consideration. Typically the distance of the closest vector from the surface is approximately 10 mm, half the size of a measurement cell. The velocity at approximately 5 mm from the wall (dilated surface) is estimated by interpolation, using two layers of closest velocity vectors. The 3D streamlines pattern on the dilated surface is inspected to reveal the relevant topological features at the surface. The velocity magnitude along the streamlines provides additional information on the flow. The near-surface friction lines are shown in Fig. 14 and more completely inspected in the supplemental material (video 4) where also the streamlines in the airflow off the surface are depicted.

The flow on the rider's back appears to separate only at the sides of the low back region. The air captured in the chest region exits sideways along the lower torso and streams towards the centre of the lower back. On the straight leg side, the separation occurs only at the gluteus as indicated by the interruption of skin friction lines from the side of the upper leg. Separation past both arms on their upper side is also evident with the sudden drop in velocity and the interruption

Fig. 14 Velocity magnitude contour at 5 mm distance to cyclist’s body and estimation of skin friction lines over the dilated surface. Three-dimensional inspection available with video 4



of the streamlines. A long separation line is drawn along the upper leg and the calf region also with the presence of two foci at the lower gluteus and in the middle of the calf respectively. No apparent separation is detected in the lower leg towards the ankle. On the right side, the flow passes the bent leg with no distinct separation in the rear of the inclined upper leg. At the right lower back flow separation is indicated by a strong velocity deficit and the interruption of streamlines. Another separation region is visible in the right knee pit and

the upper calf region of the right leg. The extent of the velocity deficit on the inclined leg appears smaller as compared to the straight left leg suggesting a condition of maximum aerodynamic resistance for the latter (Crouch et al. 2014).

4.3 Vorticity distribution and vortex skeleton

The analysis of vorticity is focussed on flow structures oriented along the streamwise direction. Iso-surfaces of

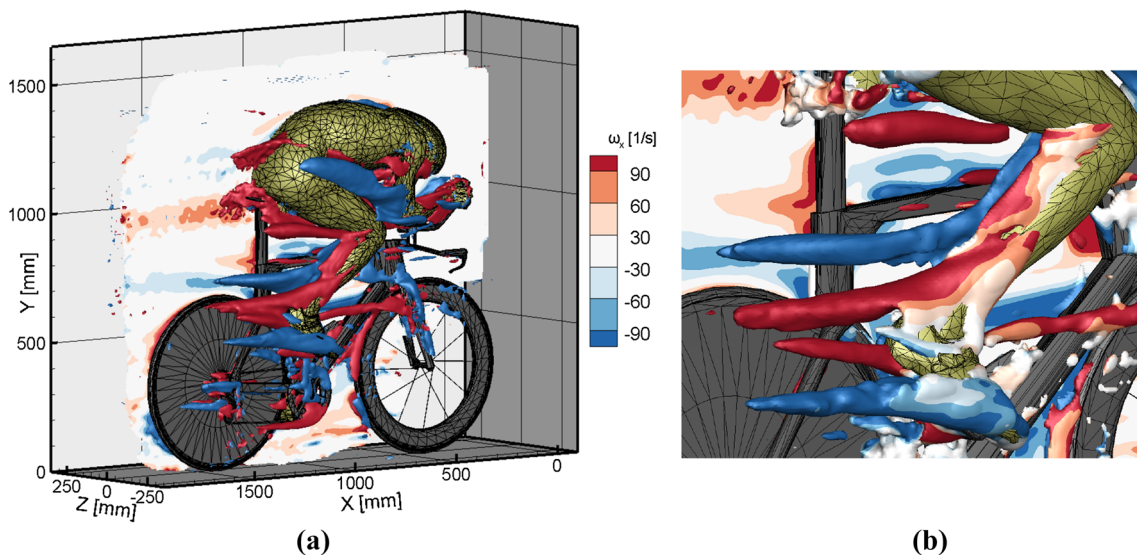


Fig. 15 Flow topology visualization by vorticity and Q-criterion. **a** Contour plane of streamwise vorticity ω_x at $z=10$ mm, together with iso-surfaces of $\omega_x = \pm 100$ s⁻¹. **b** Zoom onto right shank showing iso-

surfaces of Q-criterion coloured by ω_x . Three-dimensional inspection from movie 5

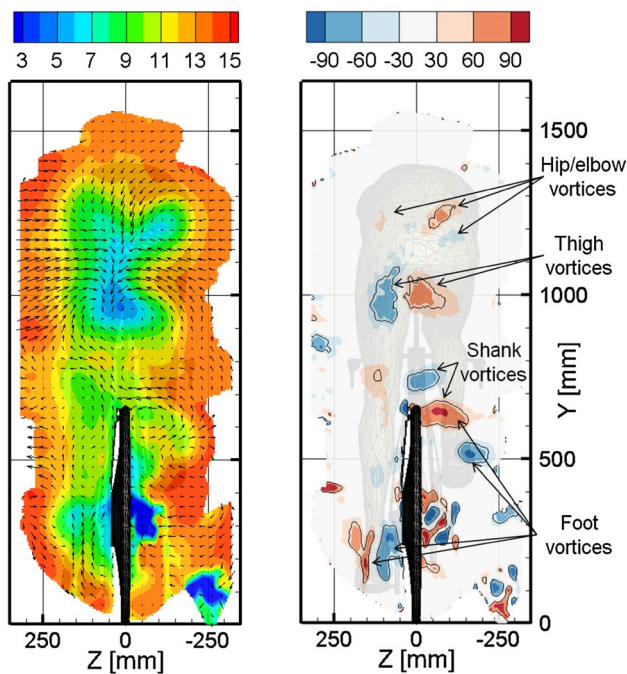


Fig. 16 Contour slices of **a** streamwise velocity u (m/s) including in-plane velocity vectors and **b** x -vorticity ω_x (s^{-1}) with contours of $\omega_x = 50 \text{ s}^{-1}$. Both planes at $x = 1500 \text{ mm}$

streamwise vorticity at $\pm 100 \text{ s}^{-1}$ are illustrated in Fig. 15—left (the full 3D distribution of streamwise vorticity is shown in video 5). Regions with anticlockwise rotation are depicted in red (positive vorticity) and clockwise in blue. The first main feature is a clockwise rotating (blue) vortex originating from the right arm and developing along the upper right leg. A pair of vortices is observed trailing from the right foot, whereas another pair of vortices is formed at the foot tip. The whole system features a vorticity quadrupole. Details of small streamwise vortices are given in video 5 as formed at several parts of the rider and of the bicycle. The smallest size of these vortex details is approximately 4 cm, which confirms the order of magnitude estimated for the DSR of the present measurements.

4.4 Momentum deficit and circulation in the near wake

Previous works have characterised the near and far wake of cyclists and inferred from a cross section in the wake that the vortex structures dominate the flow development. Here, a plane is selected in the near wake at $x = 1500 \text{ mm}$ (300 mm downstream of the lower back of the cyclist).

The velocity contour in Fig. 16 draws the detailed boundary of the wake region developed downstream of the rider. The momentum deficit is larger on the stretched-leg side, which is consistent with the thin-volume PTV measurements

of Terra et al. (2016). A strong downwash is produced by the curved back of the rider, as also found by Crouch et al. (2014) via multi-hole pressure probe measurements. The wake consists of a complex system of vortices, of which many are present below the rider's torso. Two counter-rotating vortices emanate from the inner thighs and contribute to the downwash in between them, as also reported by Crouch et al. (2014) and Terra et al. (2016). A pair of counter-rotating vortices is produced also by the foot of the stretched leg, which agrees well with the RANS simulations of Griffith et al. (2014) at 75° crank angle. As reported by Terra et al. (2016), further streamwise vortices emanate from the foot and the shank of the bent leg. Weaker and smaller vortices are present in upper part of the model, which are ascribed to the interaction of the upcoming flow with the rider's hip and elbows.

5 Conclusions

A novel approach for measuring large-scale complex aerodynamic flows has been proposed and applied to the aerodynamic analysis of a full-scale cyclist. The approach is based on the combination of coaxial volumetric velocimetry and robotics. The compact CVV technology provides improved optical access and it eliminates the need for re-calibration following a probe movement. The combination with a collaborative robot arm yields the capability to rapidly partition a large fluid domain into multiple adjacent sub-volume measurements.

The advantages of the proposed system are demonstrated in a full-scale volumetric PIV study of a time-trialling cyclist. An unprecedented ensemble of 450 time-resolved volumetric PIV acquisitions composes the time-averaged velocity field on a 2 m^3 domain around the cyclist replica. The observed flow topology features compare well to available literature and add information in the regions near the athletes' body (skin friction lines and vortices emanating from the separated regions), where the effect of changing posture or specific garments are more pronounced.

Although the improved practicality of the robotic approach for PIV system is proven, the measurement process can be further streamlined if this technique is coupled with automated object scanning algorithms. Also the detailed optimization of the measurement domain scanning, e.g. minimizing flow intrusiveness has the potential to further accelerate the acquisition process and possibly reduce the number of measurements required as volume overlap can be minimized.

Acknowledgements The provision of the hardware by LaVision, and in particular the contributions of Bernd Wieneke and Dirk Michaelis to the successful completion of this work are kindly honoured.

Open Access This article is distributed under the terms of the Creative Commons Attribution 4.0 International License (<http://creativecommons.org/licenses/by/4.0/>), which permits unrestricted use, distribution, and reproduction in any medium, provided you give appropriate credit to the original author(s) and the source, provide a link to the Creative Commons license, and indicate if changes were made.

References

- Agüera N, Cafiero G, Astarita T, Discetti S (2016) Ensemble 3D PTV for high resolution turbulent statistics. *Meas Sci Technol* 27(12):124011
- Cardano D, Carlino G, Cogotti A (2007) PIV in the car industry: state-of-the-art and future perspectives. Part Image Velocim, Springer, Berlin, pp 363–376
- Caridi GCA, Ragni D, Sciacchitano A, Scarano F (2015) A seeding system for large-scale Tomographic PIV in aerodynamics. In: 11th international symposium on particle image velocimetry, Santa Barbara, 14–16 Sept 2015
- Caridi GCA, Ragni D, Sciacchitano A, Scarano F (2016) HFSB-seeding for large-scale tomographic PIV in wind tunnels. *Exp Fluids* 57(12):190
- Casper M, Lemke C, Dierksheide U (2016) PIV in large wind tunnel by HFSB and STB. https://www.researchgate.net/profile/Uwe_Dierksheide/. Accessed 30 Mar 2017
- Colgate JE, Wannasuphprasit W, Peshkin MA (1996) Cobots: robots for collaboration with human operators. In: Proceedings of the international mechanical engineering congress and exhibition, Atlanta, DSC-vol. 58, 17–22 Nov 1996, pp 433–439
- Coustols E, Jacquin L, Moëns F, Molton P (2004) Status of ONERA research on wake vortex in the framework of national activities and European collaboration. European congress on computational methods in applied sciences and engineering—ECCOMAS 2004, Jyväskylä, 24–28 July 2004
- Crouch TN, Burton D, Brown NAT, Thompson MC, Sheridan J (2014) Flow topology in the wake of a cyclist and its effect on aerodynamic drag. *J Fluid Mech* 748:5–35
- Crouch TN, Burton D, Thompson MC, Brown NAT, Sheridan J (2016) Dynamic leg-motion and its effect on the aerodynamic performance of cyclists. *J Fluids Struct* 65:121–137
- Depardon S, Lasserre JJ, Boueilh JC, Brizzi LE, Borée J (2005) Skin friction pattern analysis using near-wall PIV. *Exp Fluids* 39(5):805–818
- Elsinga GE, Scarano F, Wieneke B, van Oudheusden BW (2006) Tomographic particle image velocimetry. *Exp Fluids* 41(6):933–947
- Griffith MD, Crouch T, Thompson MC, Burton D, Sheridan J, Brown NA (2014) Computational fluid dynamics study of the effect of leg position on cyclist aerodynamic drag. *J Fluids Eng* 136(10):101105
- Jenkins LN, Yao CS, Bartram SM, Harris J, Allan B, Wong O, Mace WD (2009) Development of a large field-of-view PIV system for rotorcraft testing in the 14-x 22-foot subsonic tunnel. AHS international 65th forum and technology display. Grapevine, TX, 27–29 May 2009
- Lignarolo LEM, Ragni D, Krishnaswami C, Chen Q, Ferreira CS, Van Bussel GJW (2014) Experimental analysis of the wake of a horizontal-axis wind-turbine model. *Renew Energy* 70:31–46
- Mead CJ, Wrighton C, Britchford K (2015) An experimental study of coaxial jets using acoustic PIV and LDA methods (CoJeN). In: 21st AIAA/CEAS aeroacoustics conference, p 3122
- Nakagawa M, Michaux F, Kallweit S, Maeda K (2015) Unsteady flow measurements in the wake behind a wind-tunnel car model by using high-speed planar PIV. In: 11th international symposium on particle image velocimetry, Santa Barbara, 14–16 Sept 2015
- Pengel K, Kooi JW, Raffel M, Willert C, Kompenhans J (1997) Application of PIV in the large low speed facility of DNW. In: New results in numerical and experimental fluid mechanics. Vieweg + Teubner Verlag, pp 253–258
- Raffel M, Richard H, Ehrenfried K, Van der Wall B, Burley C, Beaumier P, McAlister K, Pengel K (2004) Recording and evaluation methods of PIV investigations on a helicopter rotor model. *Exp Fluids* 36(1):146–156
- Scarano F (2013) Tomographic PIV: principles and practice. *Meas Sci Technol* 24(1):012001
- Scarano F, Ghaemi S, Caridi GCA, Bosbach J, Dierksheide U, Sciacchitano A (2015) On the use of helium-filled soap bubbles for large-scale tomographic PIV in wind tunnel experiments. *Exp Fluids* 56(2):42
- Schanz D, Gesemann S, Schröder A, Wieneke B, Novara M (2012) Non-uniform optical transfer functions in particle imaging: calibration and application to tomographic reconstruction. *Meas Sci Technol* 24(2):024009
- Schanz D, Huhn F, Gesemann S, Dierksheide U, van de Meerendonk R, Manovski P, Schröder A (2016a) Towards high-resolution 3D flow field measurements at the cubic meter scale. In: 18th international symposium on applications of laser techniques to fluid mechanics, 4–7 July 2016, Lisbon
- Schanz D, Gesemann S, Schröder A (2016b) Shake-The-Box: Lagrangian particle tracking at high particle image densities. *Exp Fluids* 57(5):1–27
- Schneiders JFG, Jux C, Sciacchitano A, Scarano F (2018) Coaxial volumetric velocimetry. *Meas Sci Technol*. <https://doi.org/10.1088/1361-6501/aab07d>
- Sciacchitano A, Scarano F (2014) Elimination of PIV light reflections via a temporal high pass filter. *Meas Sci Technol* 25(8):084009
- Soloff SM, Adrian RJ, Liu ZC (1997) Distortion compensation for generalized stereoscopic particle image velocimetry. *Meas Sci Technol* 8(12):1441
- Terra W, Sciacchitano A, Scarano F (2016) Evaluation of aerodynamic drag of a full-scale cyclist model by tracking particle velocimetry. In: International workshop on non-intrusive optical flow diagnostics, Delft, 25–26 Oct 2016
- Toyota Motorsports GmbH (2017). Toyota Motorsport wind tunnel helps automotive engineers design faster high-performance cars with sophisticated built-in PIV system. https://www.toyota-motor-sport.com/media/tmg/Tecplot_PIV.pdf. Accessed 19 Apr 2017
- Universal Robots A/S (2014) UR5/CB3 user manual. https://www.universal-robots.com/media/8704/ur5_user_manual_gb.pdf. Accessed 27 Mar 2017
- Wendt V, Förl M (2001) Flow field measurements around a car using particle image velocimetry. In: 4th international symposium on particle image velocimetry, Göttingen
- Wieneke B (2008) Volume self-calibration for 3D particle image velocimetry. *Exp Fluids* 45(4):549–556
- Wieneke B (2012) Iterative reconstruction of volumetric particle distribution. *Meas Sci Technol* 24(2):024008